Local seismicity near the actively deforming Corbetti volcano in the Main Ethiopian Rift

Aude Lavayssière[1], Tim Greenfield[1,2], Derek Keir[1,3], Atalay Ayele[4], J-Michael Kendall[5]

[1]Ocean and Earth Science, National Oceanography Centre Southampton, University of Southampton, Southampton, UK

[2] Bullard Laboratories, University of Cambridge, Cambridge, UK

[3]Dipartimento di Scienze della Terra, Università degli Studi di Firenze, Florence, Italy

[4] Institute for Geophysics Space Science and Astronomy, Addis Ababa University, Addis Ababa, Ethiopia

[5] Department of Earth Sciences, University of Bristol, Bristol, UK

Corresponding author:
Aude Lavayssière
Aude.Lavayssiere@noc.soton.ac.uk
25 Pacific Close, Ocean Village, SO143TX Southampton, United Kingdom

Declarations of interest: none.

Abstract

Corbetti is currently one of the fastest uplifting volcanoes globally, with strong evidence from geodetic and gravity data for a subsurface inflating magma body. A dense network of 18 stations has been deployed around Corbetti and Hawassa calderas between February 2016 and October 2017, to place seismic constraints on the magmatic, hydrothermal and tectonic processes in the region. We locate 122 events of magnitudes between 0.4 and 4.2 using a new local velocity model. The seismicity is focused in two areas: directly beneath Corbetti caldera and beneath the city of Hawassa. The shallower 0-5 km depth below sea level (b.s.l.) earthquakes beneath Corbetti are mainly focused in EW- to NS-elongated clusters at Urji and Chabbi volcanic centres. This distribution is interpreted to be mainly controlled by a northward propagation of hydrothermal fluids away from a cross-rift pre-existing fault. Source mechanisms are predominantly strike-slip and different to the normal faulting away from the volcano, suggesting a local rotation of the stress-field. These observations, along with a low Vp/Vs ratio, are consistent with the inflation of a gas-rich sill, likely of silicic composition, beneath Corbetti. In contrast, the seismicity beneath Hawassa extends to greater depth (16 km b.s.l.). These earthquakes are focused on 8-10 km long segmented faults, which are active in seismic swarms. One of these swarms, in August 2016, is focused between 5 and 16 km depth b.s.l. along a steep normal fault beneath the city of Hawassa, highlighting the earthquake hazard for the local population.

Keywords: (max 6)

East African Rift; Corbetti volcano; local seismicity; Main Ethiopian Rift; continental tectonics

1 Introduction

Seismicity in the East African Rift has previously been linked to tectonic faulting and magmatic processes (Ebinger et al., 2008; Grandin et al., 2011; Greenfield et al., 2018; Lavayssière et al., 2019; Wilks, Kendall, et al., 2017). The earthquake patterns commonly highlight rift segments and volcanic centres (map inset, Figure 1), and can be used to reveal faults systems and migration of fluids or magma beneath active volcanoes. Despite improvements in monitoring, how individual magmatic systems modify and interact with tectonic faulting in discrete portions of the rift remain poorly understood. This is particularly the case for the central Main Ethiopian Rift (MER) (Figure 1), since a previous lack of dense seismic networks means that very few earthquakes have been detected.

The Main Ethiopian Rift (MER) is a magmatically active portion of the East African Rift System (EARS) that lies between the Afar depression in the north and the Turkana depression in the south (Figure 1). The MER includes nearly 60 volcanoes that are thought to have erupted in the past 10,000 years, of which Corbetti, Bora, Aluto and Haledebi are actively deforming (Biggs et al., 2011). In particular, Corbetti is currently uplifting at 7 cm per year (Lloyd, Biggs, Birhanu, et al., 2018), making it one of the fastest deforming volcanoes on Earth. In addition, recent earthquake activity near Corbetti has been significant. On the 24th January 2016, a Mw 4.3 normal slip earthquake occurred south of Corbetti that was widely felt in the town of Hawassa (Figure 1) (Wilks, Ayele, et al., 2017) . Volcanoes in the MER have the potential to be used for geothermal energy, a resource that is starting to be exploited in Ethiopia on Aluto and Corbetti volcanoes

(Gíslason et al., 2015; Kebede, 2014). Hydrothermal systems are likely in volcanic fields due to the interaction of the subsurface magma plumbing system with the ground water.

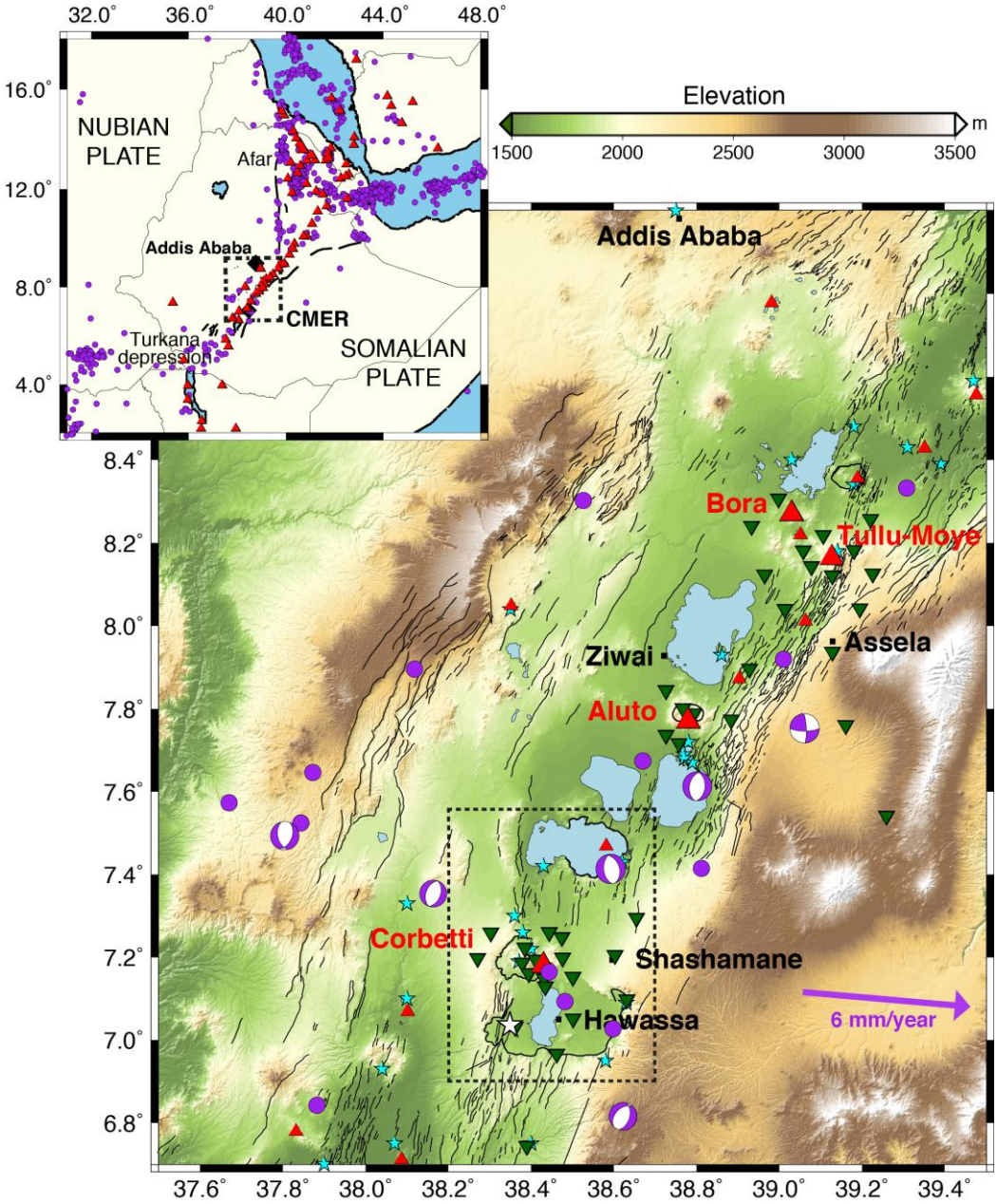

Figure 1: Map of the central Main Ethiopian Rift (CMER) with National Earthquake Information Centre (NEIC) events catalog (1976 – 2018; purple circles) and Centroid Moment Tensor (CMT) source mechanisms catalog (purple focal mechanisms). The white star represent the location of the 24th January 2016 earthquake (Wilks, Ayele, et al., 2017). The map inset shows the CMER (dashed rectangle) in the context of the northern East African Rift. Black squares indicate the main cities. Green inverted triangles are the seismic stations. Red triangles are volcanic centres with the main volcanoes in the CMER named. Black lines represent mapped faults (Agostini et al., 2011; Corti et al., 2013). Cyan stars highlight hydrothermal vents and wells. The dashed rectangle is the area shown in Figures 2 and 4. Purple arrow is the extension direction (Stamps et al., 2018).

Here we present a detailed study of the local seismicity at the Corbetti and Hawassa calderas, following the January 2016 earthquake. Using a dense network deployed across the region and generating a local seismic velocity model, we detect and precisely locate seismicity beneath a deforming caldera and nearby active rift valley faults. Local seismicity is used to understand magma and hydrothermal pathways beneath Corbetti volcano and show active faulting beneath rift valley faults.

2 Geological and geophysical setting

The MER is characterized by several *en-echelon* magmatic segments and volcanic centres associated with continental extension between the Nubian and Somalian plates (Figure 1; Ebinger & Casey, 2001). The MER is rifting at approximately 6 mm/year in a near east-west direction (Figure 1; Saria et al., 2014; Stamps et al., 2018). Extension is thought to have started in the Miocene (Wolfenden et al., 2004) and its basins were initially bounded by large border faults that accommodated the majority of the extension. The transition to magma-assisted rifting at 2 Ma (Wolfenden et al., 2004) formed short and *en-echelon* NNE-SSW intra-rift faults, including the present-day Wonji Fault Belt (WFB) along the rift valley floor of the MER (Agostini et al., 2011; Corti et al., 2013; Ebinger & Casey, 2001; Pizzi et al., 2006). This structure is interspersed by Quaternary to Recent volcanic centres such as Boset, Bora, Aluto and Corbetti (Ebinger & Casey, 2001). Although known to be seismically active, only few earthquakes have been detected in the central MER, mostly normal faulting events at border faults and events near volcanic centres (Figure 1).

Corbetti volcano is considered as one of the most frequently active volcanoes in East Africa in term of moderate-scale explosive eruptions with 1 to 3 eruptions per thousand years (Fontijn et al., 2018). Its caldera is 10 by 15 km (Hutchison et al., 2016), and elongate at an orientation of 097° (Lloyd et al., 2018) (Figure 2). The Corbetti silicic centre has a three-stage volcanic history (Fontijn et al., 2018; Di Paola, 1971) with effusive and explosive activity separated by a caldera collapse at 182 ± 18 ka. It has been highly active in the Late Quaternary with eruptions up to VEI 4-5 (Fontijn et al., 2018).

Two major centres of resurgent volcanisms, Urji (also called Wendo Koshe) and Chabbi (Mohr, 1966; Di Paola, 1971), have both erupted pantellerites. Urji is mainly composed of pumice flows, highlighting explosive activity, whereas Chabbi is composed of obsidian flows, highlighting contrasting effusive eruptions (Mohr, 1966; Rapprich et al., 2016). The last Plinian eruption at Urji occurred around 396 BC and dispersed deposits over 1000 km^2 with ~50 cm of deposits in Shashamene and more than 10 cm in Hawassa, enough to cause widespread disruption (Fontijn et al., 2018; Rapprich et al., 2016). At least four obsidian and 9 explosive eruptions post-date this massive activity (Fontijn et al., 2018; Rapprich et al., 2016).

Geological and geophysical evidence suggest that Corbetti remains seismically and magmatically active and may erupt in the future. Satellite imaging has shown significant surface deformation over the past twenty years (Biggs et al., 2011; Lloyd, Biggs, Birhanu, et al., 2018). InSAR observations show periods of uplift and subsidence between 1997 and 2010 (Biggs et al., 2011) and continuous uplift at a rate of ~7 cm/year since 2009 (Biggs et al., 2011; Lloyd, Biggs, Birhanu, et al., 2018). Lloyd, Biggs, Birhanu, et al. (2018) show that the recent continuous uplift is a

response to a volume change of ~10^7 m^3/year of magma intruding into a pre-existing reservoir at ~6.6 km depth below surface.

Deformation studies also highlight structures that control magmatic and tectonics processes. Lloyd, Biggs, Wilks, et al. (2018) and Korme et al. (2004) observe a linear feature cross-cutting the caldera coincidentally with the caldera long axis (Figure 2). This fault structure is interpreted to control the migration of magma and hydrothermal fluids to the surface, visible by the alignment of post-caldera vents (Lloyd, Biggs, Wilks, et al., 2018).

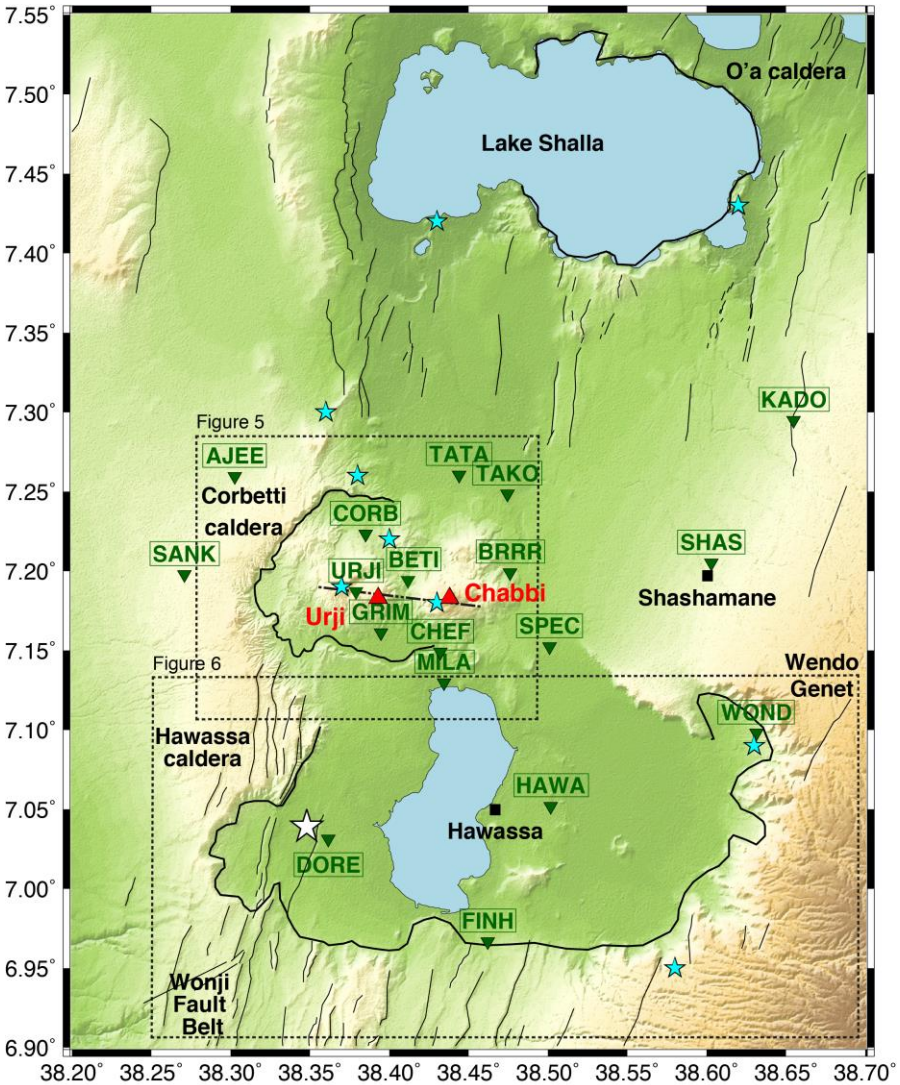

Figure 2: Map of the seismic network. Black squares represent the main cities. Main volcanic centres are named and located as red triangles. The black dashed line crossing Corbetti caldera represents a cross-rift fault structure (Lloyd, Biggs, Wilks, et al., 2018). Cyan stars highlight hydrothermal vents and wells. Green inverted triangle are stations with their associated name. The white star is the location of the 24th January 2016 earthquake (Wilks, Ayele, et al., 2017). Dashed rectangles are sub-regions explored in this study (Figures 5 and 6).

Magnetotelluric and resistivity measurements around Corbetti indicate a sharp resistivity change along the caldera long-axis at 0-2 km below surface and another at depth greater than 10 km below surface (Gíslason et al., 2015). The shallow change in resistivity is thought to be a buried strike-slip fault, coincident to the fault structure identified by Lloyd, Biggs, Wilks, et al. (2018), controlling migration of hot hydrothermal fluids to the northern half of the caldera (Gíslason et al., 2015). On the surface, this hydrothermal system consists of numerous fumaroles and thermally altered soils. The deep conductive layer has been interpreted as a possible magma body (Gíslason et al., 2015).

Little is known about the seismicity and crustal structure of the Corbetti caldera. Regional studies have constrained the crustal structure of the MER (Daly et al., 2008; Keir, Ebinger, et al., 2006) and local studies have identified seismically active structures at the nearby volcanic fields of Tullu-Moye (Greenfield et al., 2018) and Aluto (Wilks, Kendall, et al., 2017). Previous monitoring of local seismicity at Corbetti has been done in 2012-2014 with a sparse network of seven stations (Lloyd, Biggs, Birhanu, et al., 2018; Lloyd, Biggs, Wilks, et al., 2018). It showed dispersed seismicity with events located between Chabbi and Urji down to 9 km depth and a large number of events at Wendo Genet, east of Hawassa caldera (Lloyd, Biggs, Birhanu, et al., 2018; Lloyd, Biggs, Wilks, et al., 2018) (Figure 2). However, the velocity model used in these earlier works was a regional 1D velocity model of the MER (Daly et al., 2008).

Teleseismically detected earthquakes are infrequent in this area of the rift with only 5 events detected within 50 km of Corbetti (Figure 1). The most recent event occurred on the 24th January 2016, immediately before the seismic network was deployed. The magnitude 4.68 earthquake (Wilks, Ayele, et al., 2017) was large enough to be felt up to 100 km away and caused damage to buildings in the city of Hawassa that hosts a population of ~320,000 people. The event was located to the southwest of Hawassa at a depth of 4.55 km depth using regional stations > 200 km away from the hypocentre (Wilks, Ayele, et al., 2017) (Figure 2). The earthquake focal mechanism reveals that the event is a normal slip on a north-south-striking fault associated with the caldera rim of the Hawassa caldera (Wilks, Ayele, et al., 2017).

South of Corbetti, the Quaternary Hawassa caldera is located at the eastern escarpment of the rift, forming an EW-elongated, 35 by 20 km, topographic depression, filled by the 92 km^2 Lake Hawassa (Figure 2). The caldera is composed of silicic lava flows, pumices and welded tuff dated at 1.85-1.1 Ma, and has also been filled by products of more volcanic activities associated with the formation of Corbetti volcano (Mohr et al., 1980; Di Paola, 1971; WoldeGabriel et al., 1992). It has been affected by NS-trending faults that formed a down-faulted central sector where Lake Hawassa is located (Boccaletti et al., 1998) (Figure 2).

North of Corbetti is located one of the largest calderas in the central Main Ethiopian Rift, the O'a caldera (120 km^3; Mohr et al., 1980) (Figure 2). It contains the volcanically and tectonically controlled Lake Shalla (Le Turdu et al., 1999). Observations show ESE-trending transverse faults

with 5 to 30 m throw on the eastern caldera walls (Mohr et al., 1980; Le Turdu et al., 1999) but the deep structure beneath Lake Shalla and the O'a caldera remains unknown.

3 Data and Methods

3.1 Seismic network and earthquake detection

37 stations were deployed across the MER (Figure 1), including 18 installed around Corbetti and Hawassa calderas, in February 2016 (Figure 2). The network consists of 3-component, broadband instruments: 25 Guralp CMG-6TD and 12 Guralp CMG-ESPCD seismometers, recording at 50 samples per second. The instruments were removed in October 2017, yielding 1.5 years of data.

Earthquakes were detected using the Coalescence Microseismic Mapping (CMM) technique (Drew et al., 2013). We generate our catalogue using only events with signal-to-noise ratio above 3. A total of 286 events were detected using these parameters over the duration of the experiment. To improve the accuracy of the phase arrival times we manually refine a total of 3450 P-wave and 3641 S-wave arrival times using the entire network of 37 stations.

3.2 Velocity model

Accurate earthquake locations depend on having a good knowledge of the subsurface velocity structure of the study area. In order to develop a sensible velocity model for the region we invert the arrival time results with the program *Velest* (Kissling et al., 1995). This program minimises the misfit between the arrival times and the model predictions. We use only the events that have at least 6 arrivals, including at least 2 S-arrivals, and recorded with an azimuthal gap of less than 200°. This results in a total of 173 events. Analysis of the P- and S-wave arrival time on a Wadati diagram yields a best-fit Vp/Vs ratio of 1.683 ± 0.003. Applying these criteria, we determine a minimum 1D P-wave velocity model (black curve, Figure 3) with a root-mean-square error for the velocity model of 0.232 s. Since earthquakes generally cluster in depth at sharp changes in velocity, we smooth the velocity model output from *Velest* to generate the final velocity model (red line, Figure 3). It is interesting to note that the Vp structure we image is fairly similar to the Aluto velocity model (Wilks, Kendall, et al., 2017), and slower than the Bora Tullu-Moye velocity model (Greenfield et al., 2018), particularly between ~3-8 km depth. This could be due to a thicker sedimentary basin in the shallow crust (Maguire et al. 2006), or to the crust being hotter and/or

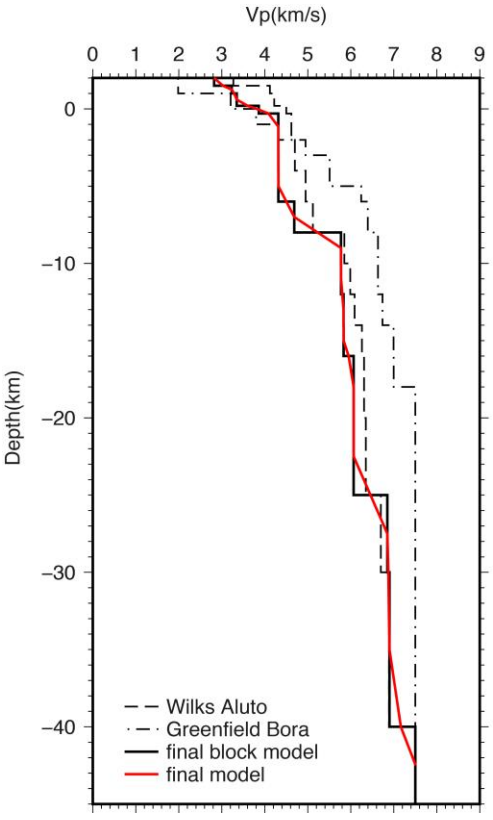

Figure 3: 1D velocity models. The final velocity model is shown in solid red and compared to previous models (dashed lines) (Wilks, Kendall, et al., 2017; Greenfield et al., 2018) and to the block model obtained from *Velest* (solid black line).

the presence of partial melt in the subsurface beneath our study area.

3.3 Earthquake location

The new velocity model is used to locate our catalogue of events with *NonLinLoc* (Lomax, 2008). This program estimates the probability density function of the hypocentre (Lomax et al., 2000; Tarantola & Valette, 1982). From the *NonLinLoc* results, we select events located within the network (gap < 180°). This results in a catalogue of 122 hypocentres, used in the subsequent analyses (Table S1).

3.4 Magnitudes

The local magnitude of the detected earthquakes (M_L) are calculated with the following equation, adapted for the MER (Keir, Stuart, et al., 2006)

$$M_L = \log A_0 + 1.196997 * \log (r / 17) + 0.001066 * (r - 17) + 2 + C$$

where A_0 is the maximum zero-to-peak amplitude corrected to the response of a Wood-Anderson seismograph, C is the station correction and r is the hypocentral distance in kilometres. Considering the low number of earthquakes used in this study we chose not to calculate the b-value of the catalogue.

3.5 Focal mechanisms

We determine focal mechanisms solutions for the 122 events within our catalogue using the *FOCMEC* program (Snoke, 1984), which assumes a double-couple solution. The take-off angle and back-azimuth from *NonLinLoc* and P-wave, first-motion polarities of the vertical waveform are used to search for nodal planes solutions. The solutions are considered good if the nodal planes have little spread (< 15°) and there is polarity data in at least 3 quadrants with no polarity errors allowed. 22 events follow these criteria and are presented in the following section.

4 Results and interpretations

The 122 well-constrained earthquake locations highlight three active regions of seismicity: beneath Lake Shalla, beneath Corbetti caldera and beneath the eastern shore of Lake Hawassa (Figure 4).

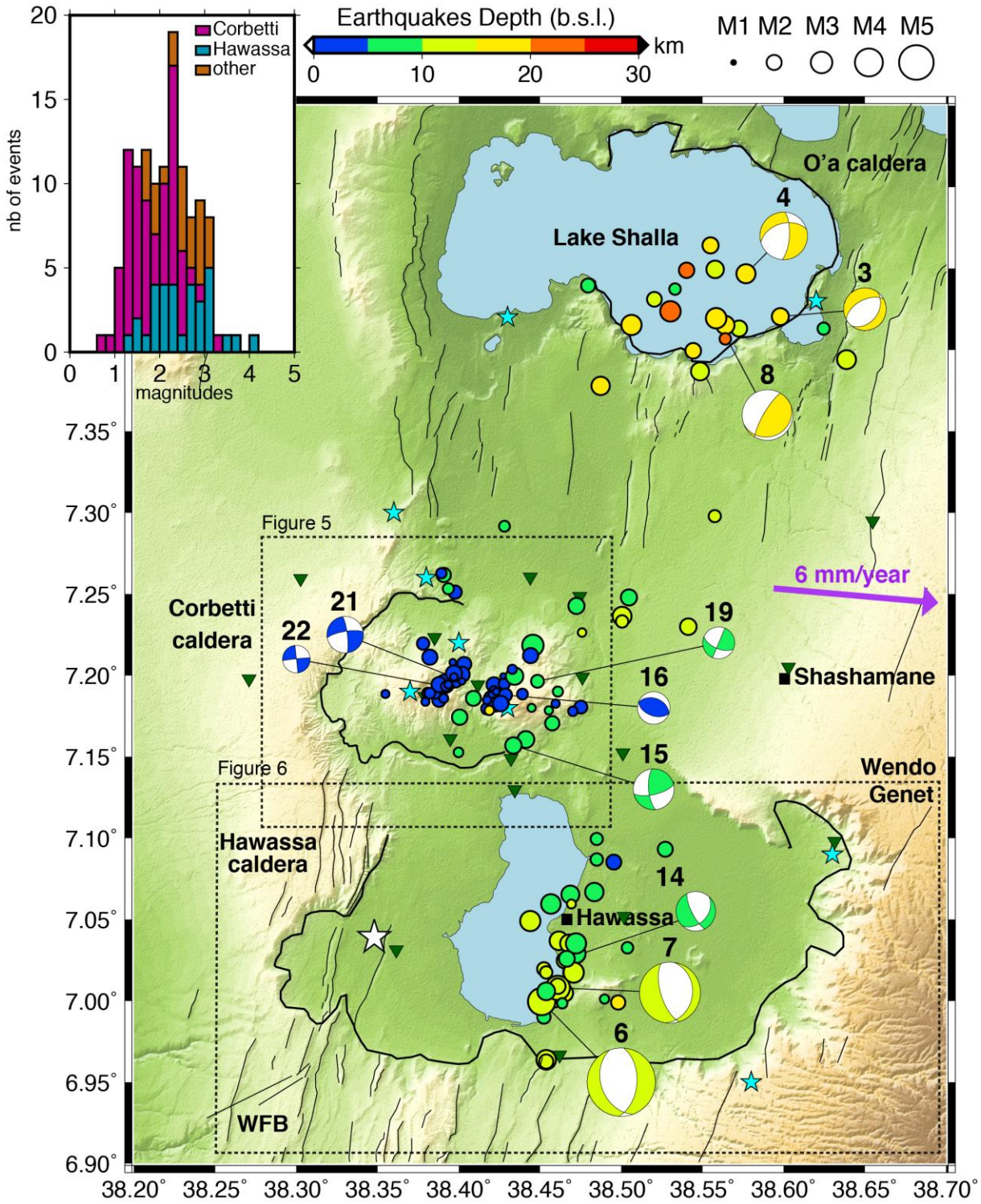

Figure 4: Map of epicentral locations (122 earthquakes) scaled to magnitude and color-coded with depth below sea level (b.s.l.). Dashed rectangles enclose sub-regions shown in Figures 5 and 6. Green inverted triangles are seismic stations. Purple arrow indicates the extension direction. Cyan stars highlight hydrothermal vents and wells. Black squares represent the main cities. The white star is the location of the 24th January 2016 earthquake (Wilks, Ayele, et al., 2017). Inset is the magnitude histogram for the events in each part of the study area.

4.1 Corbetti caldera

The seismicity located within Corbetti caldera is distributed between 0 and 10 km depth below sea level (b.s.l.). The events occur at or north of a cross-rift structure (Figure 5) (Lloyd, Biggs, Wilks, et al., 2018). Most of the 5-10 km deep events are located away from the volcano vents and aligned with the caldera rim, with the exception of two events beneath the centre of the caldera (green events, Figure 5). The shallower activity (0-5 km), however, is clustered around the northwest side of Urji and the west side of Chabbi (blue events, Figure 5). The events close to Chabbi form a NS-oriented cluster whereas the events next to Urji form three groups of earthquakes that align subparallel and perpendicular to the cross-rift structure (Figure 5). All shallow events seem enclosed by the 3 hydrothermal vents in the caldera. Note also the small group of 4 earthquakes located in the north, just outside the caldera, next to a hydrothermal vent (Figure 5).

The Corbetti earthquake activity shows no clear pattern in time and do not occur in clear swarms of activity. Their magnitudes are relatively small, between 0.6 and 3.4 (Figures 4, 5), as expected near a deforming volcano. A high geothermal gradient and the expected high fracture density inhibit generation of larger magnitude earthquakes. Most of the focal mechanisms show strike-slip faults along the caldera rim (events 1, 15, 18 and 19; Figure 5), and strike-slip and thrust mechanisms for the clusters near the vents (events 10, 16, 20, 21 and 22; Figure 5).

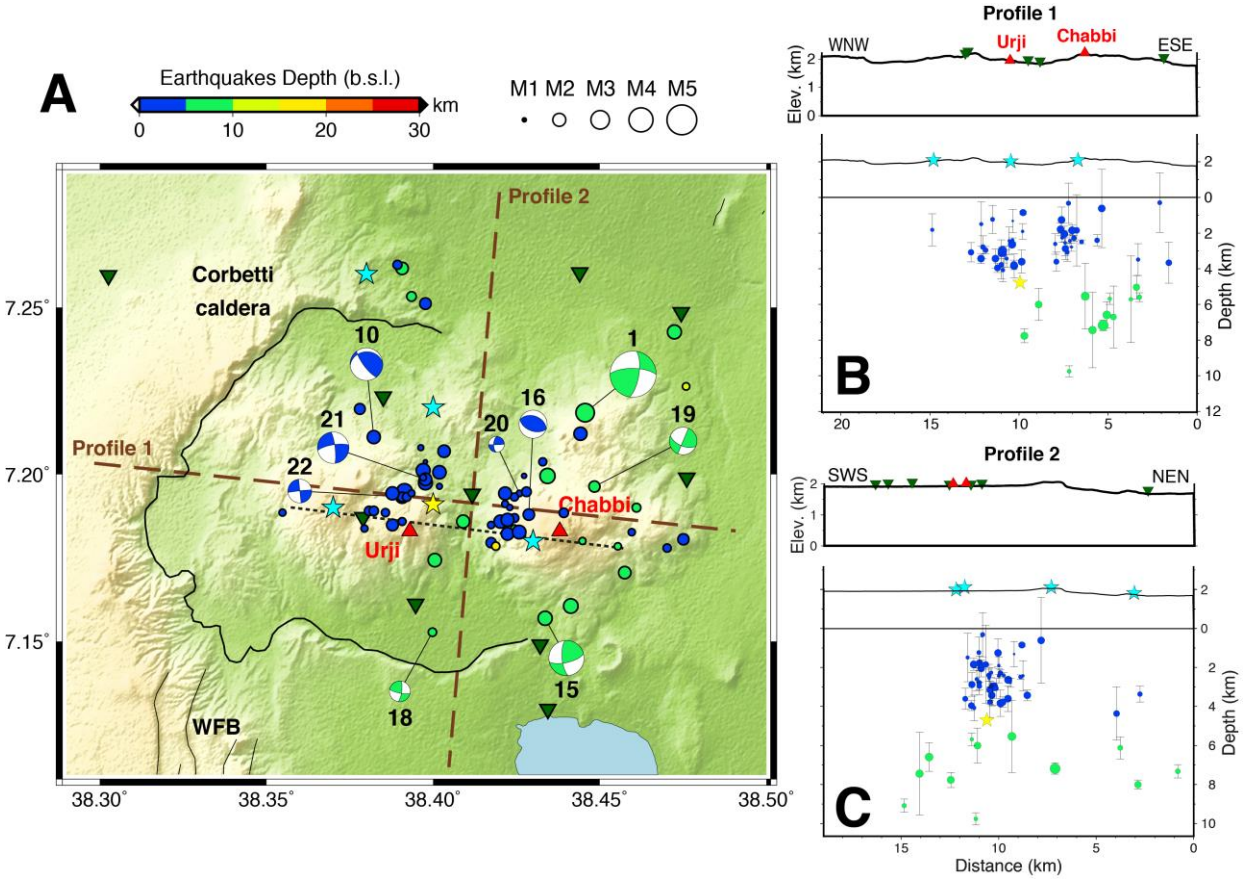

Figure 5: Corbetti volcano seismicity. **A)** Map of epicentral locations at Corbetti volcano. The events are scaled to magnitude and color-coded with depth b.s.l. Dark brown dashed lines represent traces of cross-sections shown in B

and C. The black dashed line is a cross-rift structure identified by Lloyd, Biggs, Wilks, et al. (2018). Blue ellipses highlight specific groups of earthquakes (see text for details). **B)** Profile 1 across rift axis and **C)** Profile 2 along rift axis. Green inverted triangles are seismic stations, red triangles highlight the two main volcanic centres. Cyan stars highlight hydrothermal vents and wells.

The cross-sections were made parallel (Figure 5B) and perpendicular (Figure 5C) to the extension direction to illustrate the structure at depth. Profile 1 highlights that there is no deep (> 5 km depth) seismicity beneath Urji and the west side of the caldera. The deep seismicity in the east might highlight a steep fault beneath the caldera rim. Profile 2 (Figure 5C) shows that the deep seismicity is not controlled by the cross-rift structure identified by Lloyd, Biggs, Wilks, et al. (2018). However, the shallow seismicity occurs only north of this structure.

4.2 Hawassa

The events in the Hawassa area have a magnitude range between 1.2 to 4.2 (Figures 4, 6, 7). The seismicity is distributed between 5 and 16 km depth b.s.l. along the east shore of Lake Hawassa, with most of the earthquakes located directly beneath Hawassa town (Figure 6A). The epicentral locations seem to follow the curves of the lake shoreline (Figure 6A).

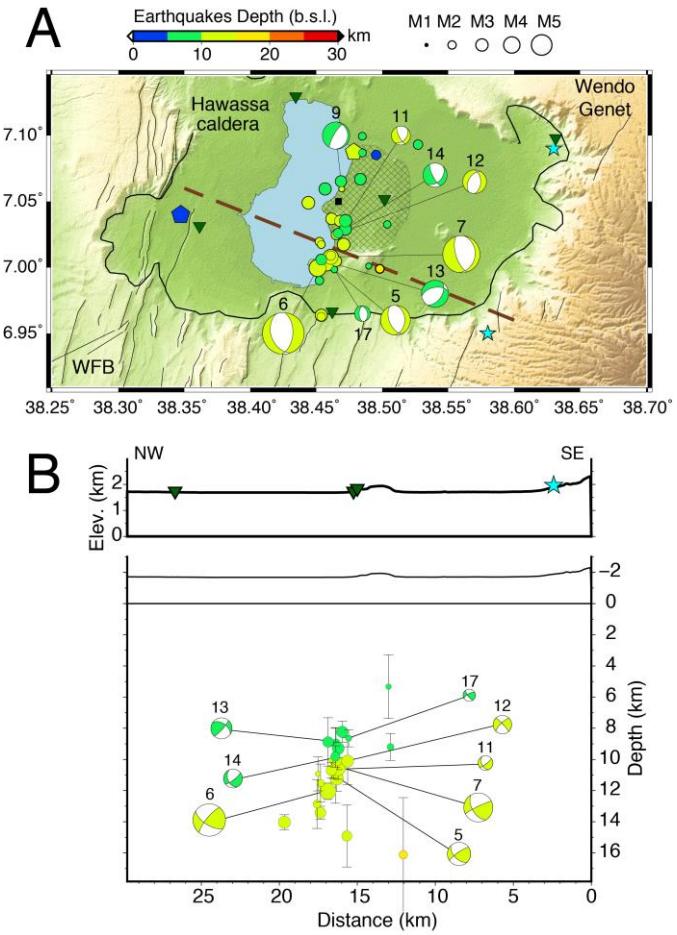

Figure 6: Hawassa seismicity. A) Map of epicentral locations near Hawassa. The events are scaled to magnitude and color-coded with depth. Dark brown dashed line represents the trace of the cross-section in B. The pentagons identify the locations of the 24th January 2016 earthquake as determined by the NEIC and Wilks, Ayele, et al. (2017). The gridded shape represents the extent of Hawassa town (black square). B) Cross-section across the August 2016 swarm. Green inverted triangles are seismic stations. Cyan stars highlight hydrothermal vents and wells.

In contrast to the Corbetti earthquakes, the Hawassa seismicity is clustered in time (Figure 7) with a small swarm of events in February 2016 mainly located on the northeast shore of Lake Hawassa, and the main swarm in August 2016 located just south of Hawassa town, on the southeast shore of Lake Hawassa (Figures 6, 7). The clusters highlight 8-10 km-length segments of activity, similar in length to fault scarps previously mapped (Agostini et al., 2011; Casey et al., 2006)(Figures 6, 7). There is a distinct absence of seismicity on the west side of the caldera where the 24th January 2016 earthquake has been located (Wilks, Ayele, et al., 2017) and in the east near Wendo Genet, a previously active region (Lloyd, Biggs, Wilks, et al., 2018) (Figures 6, 7).

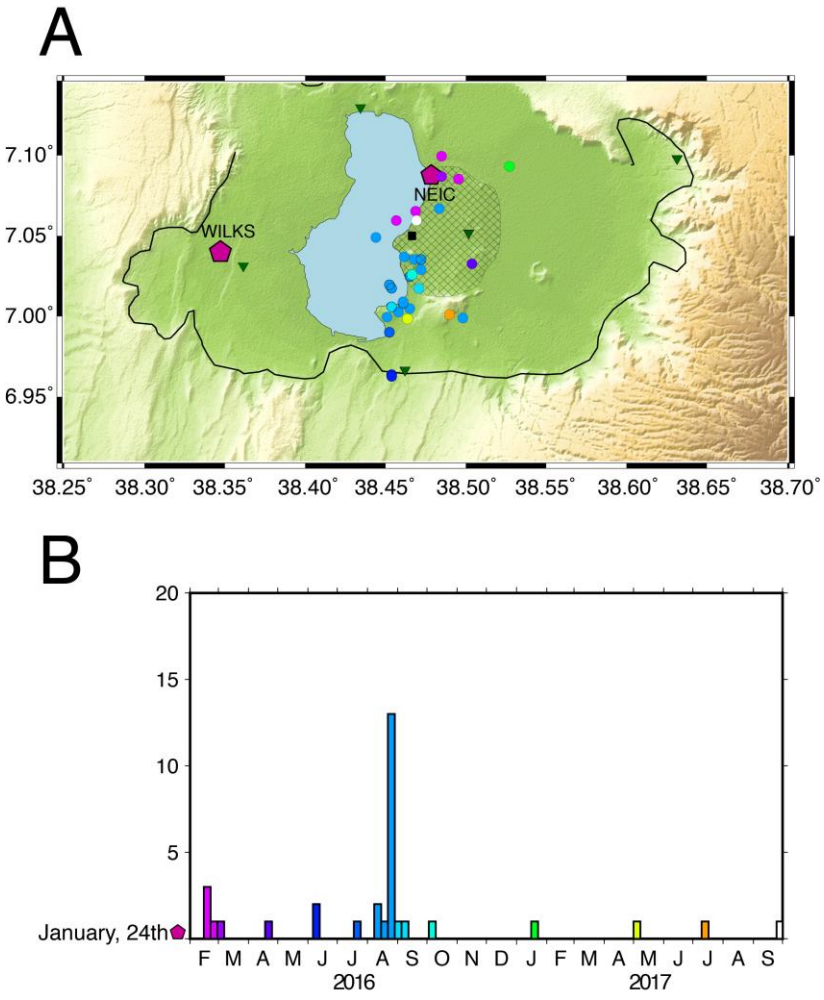

Figure 7: A) Map of epicentral locations color-coded by time as represented in B. Locations of the 24th January 2016 earthquake as identified by the NEIC and Wilks, Ayele, et al. (2017) are indicated (pink pentagons). Green inverted triangles are seismic stations. The gridded shape represents the extent of Hawassa town (black square). **B)** Time histogram of the seismicity at Hawassa. The January, 24th event is indicated (pink pentagon).

The profile in Figure 6B was made perpendicular to the August swarm and only uses events from this cluster. The distribution highlights a steep, ~75° dip, fault beneath the lake and the town of Hawassa (Figure 6B). Focal mechanisms all show normal faulting (Figure 6). Correlation with the distribution of the seismicity shows that the fault plane is likely to strike NE-SW and dip toward the west (Figure 6).

4.3 Lake Shalla

The Lake Shalla seismicity is located beneath the southeast corner of the lake and is distributed between 5 and 30 km depth b.s.l. Focal mechanism solutions indicate normal faulting along the O'a caldera wall (event 3), as well as beneath the lake (event 4) (Figure 4). The latter contains a strike-slip component. Event 8 from the central group of earthquakes show a near-vertical nodal plane in a normal mechanism (Figure 4). However, Lake Shalla and the O'a caldera are relatively far from our network, and the events' depth are not particularly well constrained.

5 Discussion

5.1 Seismogenic thickness and length of faulting

The depth distribution of earthquakes beneath Corbetti and Hawassa calderas map the seismogenic thickness in this area (Scholz, 1988; Watts & Burov, 2003). Moho depth estimates for this region of the MER vary between 30 and 37 km (Dugda, 2005; Stuart et al., 2006), and therefore beneath Hawassa the imaged fault extends to the mid-crust (16 km depth). The seismogenic thickness is similar to the maximum depth of earthquakes further north beneath the MER, constrained at < 18 km using a local seismic network (Keir, Ebinger, et al., 2006). It is also consistent with the effective elastic thickness in the MER, constrained at < 15 km by inversion of topography and gravity data (Hayward & Ebinger, 1996; Pérez-Gussinyé et al., 2009). This relatively shallow seismogenic thickness is comparable with other magmatic rifts in the EARS, such as the Afar triple junction (< 7 km) (Ayele et al., 2007; Pérez-Gussinyé et al., 2009), where the lithosphere is weaker due to intense magmatism (Daniels et al., 2014). On the contrary, regions with little to no magmatic activity have a thicker seismogenic layer (Lavayssière et al., 2019).

Earthquakes shallow significantly beneath Corbetti where the maximum earthquake depth is 12km. This shallowing of the brittle-ductile transition beneath Corbetti volcano is consistent with a locally higher geothermal gradient. Indeed, most earthquakes are clustered even shallower, above 5km depth, beneath the main volcanic centres (Figures 5, 7). This fits geodetic models constrained by InSAR and GPS observations of current surface uplift suggesting the presence of an inflating magma body at 4.6 km depth b.s.l. beneath Corbetti (Lloyd, Biggs, Wilks, et al., 2018). Hence the abrupt shallowing of the brittle-ductile transition beneath Corbetti is interpreted to be caused by magmatic processes.

Fault depth is generally scaled to fault length (Foster & Jackson, 1998; Hayward & Ebinger, 1996), relation controlled by the strength of the lithosphere. Indeed, the development of rifting involves thinning and heating of the crust, leading to a decrease in the effective elastic thickness of the

lithosphere (Hayward & Ebinger, 1996). The relatively shallow seismogenic layer thickness observed near Lake Hawassa is consistent with the length of active faults in the region. The seismicity detected near Hawassa during our deployment is spatially arranged into 8-10 km long clusters that correlate well with the length of mapped intra-rift faults (Agostini et al., 2011; Casey et al., 2006) (Figures 6, 7). Most of these faults are inactive during our experiment, apart from the two NS-striking faults on the eastern shore of Lake Hawassa. These two adjacent fault segments seem to be active during discrete time periods. The activity on one segment may change the stress field locally and induce activity on the adjacent segment (Cowie, 1998). The relatively short fault segment lengths observed at Hawassa are different to less magma-rich segments in the EARS, such as in the Tanganyika rift where seismicity defines ~30 km-long cluster along the border faults (Lavayssière et al., 2019).

5.2 Corbetti volcano

A striking feature of the local seismicity at Corbetti volcano is a distribution of clusters of shallow events beneath Urji and Chabbi and enclosed by hydrothermal vents to the north, west and east of the volcanic centres (Gíslason et al., 2015) (Figures 5, 7). These events are also located north of a previously identified cross-rift structure through Corbetti (Lloyd, Biggs, Wilks, et al., 2018) (Figures 5, 8). Previous interpretations of the fluid flow beneath Corbetti suggest that this structure acts as an impermeable barrier that forces fluids to migrate northward (Gíslason et al., 2015, Lloyd, Biggs, Wilks, et al., 2018). Hence the distribution of earthquakes is consistent with them being induced by pore pressure changes in and near the fracture system from the migration of hot upwelling fluids northward from the cross-rift structure (Figure 8). A similar interpretation of fluid motion induced by fault slip has previously been used to interpret fault-aligned clusters of microseismicity in the Asal-Goubbet rift (Doubre et al., 2007). Alternatively, the seismicity close to the reservoir could also be caused by thermally induced volume changes (contraction and dilatation) of the surrounding rocks (Doubre et al., 2007).

Measurement of Vp/Vs ratios can provide crucial subsurface constraints on rock type and fluid content (Christensen, 1996). The Vp/Vs ratio of 1.683 found for our catalogue is relatively low compared to the global average of 1.75 (Christensen, 1996) and to the 1.76 regionally constrained for the upper crust in the region (Greenfield et al., 2018; Keir, Ebinger, et al., 2006). Instead our low Vp/Vs is consistent with the presence of geothermal fluids with heated vapor in the subsurface and/or with silicic magma charged with gas at depth. A low Vp/Vs at depth is often interpreted as a magma chamber with high (55-75%) silica contents (Christensen, 1996; Zhang & Lin, 2014), with a small percent (~2%) of water content (Lin & Shearer, 2009; Nakajima et al., 2001), and/or with the presence of gas (Husen et al., 2004; Lin, 2013). This is consistent with the on-going geothermal activity (Gíslason et al., 2015) and with the silicic volcanic history at Corbetti with 75 wt% SiO2 (Fontijn et al., 2018) and a high content of chemically bound water (Rapprich et al., 2016).

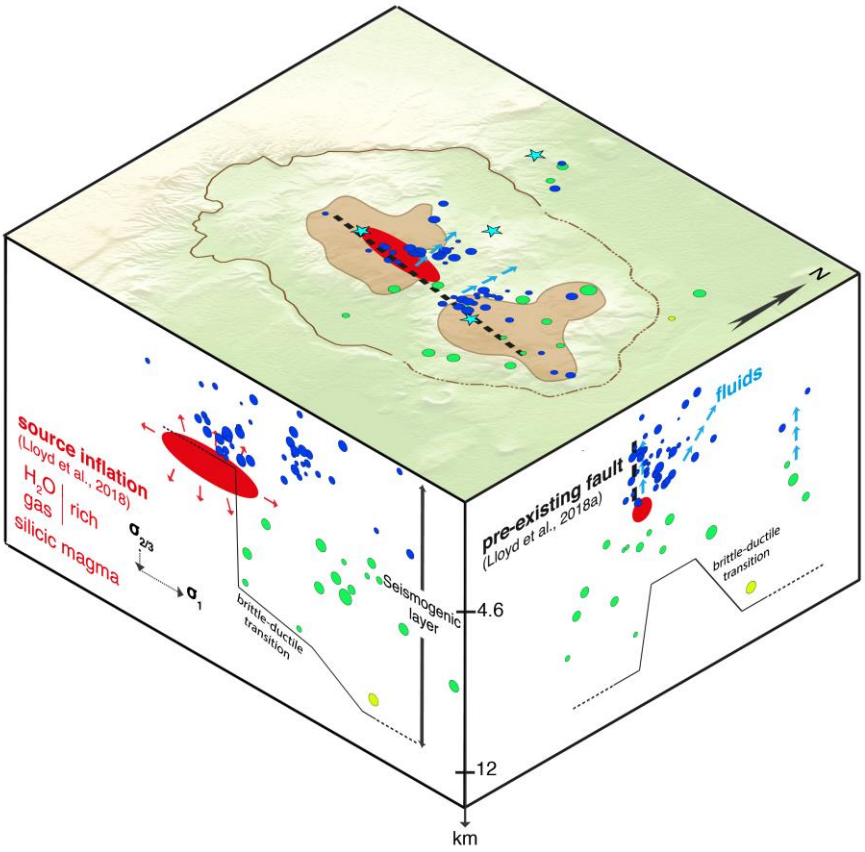

Figure 8 : 3D interpretation of Corbetti volcano seismicity. The events are scaled to magnitude and color-coded with depth b.s.l. The black dashed line represents the cross-rift structure (Lloyd, Biggs, Wilks, et al., 2018). An assumption on the depth to the brittle-ductile transition is indicated. Cyan stars highlight hydrothermal vents and wells. See text for details.

Combination of source mechanisms and shape of the earthquake's distribution can provide evidence on the position, geometry and slip style of the active fault structures. Nodal planes solutions at Corbetti are mostly EW and NS but there is no conclusive evidence for which one the fault plane is. Two groups of earthquakes in the Urji cluster seem to align in an EW orientation (Figure 5), subparallel to the cross-rift structure (Lloyd, Biggs, Wilks, et al., 2018), indicating that the EW nodal plane might be the fault plane. However, the northern group of Urji events and the Chabbi cluster are aligned NS. Hence, as they get further from the pre-existing structure, the faults seem to change strike from EW (tectonic rift-related stress field or stress due to upward fluid migration from depth) to NS (possibly related to northward fluid migration). This variation in the stress field is also evident in observations of shear-wave splitting in local events, which are interpreted in terms of fracture-induced anisotropy (Lloyd, Biggs, Wilks, et al., 2018). The anisotropy shows a roughly EW orientation south of the cross-rift structure and more NS to the north. It is plausible that the stress is perturbed by strike-slip motion and pore-pressure effects along the cross-rift fault.

The difference of focal mechanisms between Corbetti and in the rest of the rift valley show that uplift processes modify the stress-field beneath the volcano. The presence of strike-slip and thrust events at Corbetti vents can be explained by locally reducing the magnitude of the vertical stress to be lower than the regional horizontal stresses. Lloyd, Biggs, Birhanu, et al. (2018) suggest that the pressurization of a horizontal dislocation, or sill, oriented 097° and at 4.6 km depth b.s.l., fit the volume change and uplift of the caldera (Figure 8), and is consistent with our observations. The inflation of a horizontal reservoir would decrease the vertical stress and increase the horizontal stress, leading to a local change of the stress field at the volcano (Figure 8). Thus, the pressure changes due to the inflation explains the occurrence of the strike-slip events ($\sigma1$ horizontal and $\sigma2$ vertical) and thrust events ($\sigma1$ horizontal and $\sigma3$ vertical).

5.3 Earthquake hazard

The locations of earthquakes we derive for Hawassa shows seismic activity focused on a steep fault on the eastern shore of Lake Hawassa. This does not correlate with the best fitting location of the 24th January 2016 event made by Wilks, Ayele, et al. (2017), but it does correlate with the NEIC location (Figures 6, 7). Both locations were calculated using distant stations (distances > 200 km) and have large locations errors (1.8 km in latitude, 8 km in longitude and 3 km in depth; Wilks, Ayele, et al., 2017). The January event was interpreted by Wilks, Ayele, et al. (2017) to be a slip along a WFB fault, associated with the caldera rim fault of the Hawassa caldera. It correlates with previous normal faulting events in 1983 and 1995, also located at WFB faults near the caldera west wall. However, there is no evidence for any activity in this area during our period of study. In the contrary, the swarm of activity in February 2016 is located on the northeast shore of Lake Hawassa, coincident with the NEIC location of the January 2016 event. It is likely that aftershocks of the relatively large January 2016 event occurred in the following month and should have been detected by our network. This might indicate that the January event have occurred beneath the northern part of Hawassa, coincident with the February activity.

The seismicity is distributed in segments that are particularly visible near Hawassa. The segments on the east shore of Lake Hawassa follow the shape of the lake at the surface, indicating that the fault may reach the surface. Most of the seismicity is located directly beneath Hawassa town (Figures 6A, 7A), increasing the earthquake hazard in this region and showing the importance of a continuous, close monitoring of the area.

6 Conclusions

To constrain the local seismicity at a rapidly deforming volcano, and better understand magmatic, hydrothermal and fault slip processes, a dense network of 17 stations recorded 122 earthquakes at Corbetti and Hawassa calderas between February 2016 and October 2017. The events, of magnitude 0.4 to 4.2, were located using a new local velocity model. Their spatial distribution is mainly focused between Corbetti caldera and beneath Hawassa town, along the eastern shore of Lake Hawassa.

The distribution of the seismicity around Corbetti volcano is focused at shallow depths (0-5 km b.s.l.) beneath its two main volcanic centres, Urji and Chabbi. The earthquake locations are

consistent with a northward propagation of hydrothermal fluids coming from beneath Urji and propagating along a cross-rift, pre-existing structure. Source mechanisms give evidence for a local stress field change due to the inflation of a gas-rich, silicic sill with a small percent of water content in the upper crust.

The 10-km thick seismogenic layer beneath Corbetti is thinner than beneath Hawassa where it reaches 16 km, probably due to elevated temperature and fluids beneath the volcano. The deeper events beneath Hawassa are also higher magnitude and are active in swarms along 8 to 10 km-long segmented normal faults. The network used in this study detects one of these swarm in August 2016 and give evidence for a steep normal fault beneath the town of Hawassa, demonstrating the significant earthquake hazard for its population.

Acknowledgments

We thank SEIS-UK, supported by the Natural Environment Research Council (NERC) under agreement R8/H10/64, for the loan of all seismic instruments; and all person involved in fieldwork, especially our local collaborators at the Institute of Geophysics, Space Sciences and Astronomy (IGSSA) in Addis Ababa. The seismic data used in this research is stored at SEIS-UK and will be available on IRIS (https://www.iris.edu/hq/) after October 2020. The fieldwork is supported by NERC grant NE/L013932/1. We would also like to thank Pr. Robert White for the use of the CMM algorithm on the Cambridge server.

References

Agostini, A., Bonini, M., Corti, G., Sani, F., & Mazzarini, F. (2011). Fault architecture in the Main Ethiopian Rift and comparison with experimental models: Implications for rift evolution and Nubia–Somalia kinematics. *Earth and Planetary Science Letters*, *301*(3–4), 479–492. https://doi.org/10.1016/J.EPSL.2010.11.024

Ayele, A., Stuart, G., Bastow, I., & Keir, D. (2007). The August 2002 earthquake sequence in north Afar: Insights into the neotectonics of the Danakil microplate. *Journal of African Earth Sciences*, *48*(2–3), 70–79. https://doi.org/10.1016/j.jafrearsci.2006.06.011

Biggs, J., Bastow, I. D., Keir, D., & Lewi, E. (2011). Pulses of deformation reveal frequently recurring shallow magmatic activity beneath the Main Ethiopian Rift. *Geochemistry, Geophysics, Geosystems*, *12*(9). https://doi.org/10.1029/2011GC003662

Boccaletti, M., Bonini, M., Mazzuoli, R., Abebe, B., Piccardi, L., & Tortorici, L. (1998). Quatemary oblique extensional tectonics in the Ethiopian Rift (Horn of Africa). *Tectonophysics*.

Casey, M., Ebinger, C., Keir, D., Gloaguen, R., & Mohamed, F. (2006). Strain accommodation in transitional rifts: extension by magma intrusion and faulting in Ethiopian rift magmatic segments. *Geological Society, London, Special Publications*, *259*(1), 143–163. https://doi.org/10.1144/GSL.SP.2006.259.01.13

Christensen, N. I. (1996). Poisson's ratio and crustal seismology. *Journal of Geophysical Research: Solid Earth*, *101*(B2), 3139–3156. https://doi.org/10.1029/95JB03446

Corti, G., Philippon, M., Sani, F., Keir, D., & Kidane, T. (2013). Re-orientation of the extension

direction and pure extensional faulting at oblique rift margins: comparison between the Main Ethiopian Rift and laboratory experiments. *Terra Nova*, *25*(5), 396–404. https://doi.org/10.1111/ter.12049

Cowie, P. A. (1998). A healing–reloading feedback control on the growth rate of seismogenic faults. *Journal of Structural Geology*, *20*(8), 1075–1087. https://doi.org/10.1016/S0191-8141(98)00034-0

Daly, E., Keir, D., Ebinger, C. J., Stuart, G. W., Bastow, I. D., & Ayele, A. (2008). Crustal tomographic imaging of a transitional continental rift: the Ethiopian rift. *Geophysical Journal International*, *172*(3), 1033–1048. https://doi.org/10.1111/j.1365-246X.2007.03682.x

Daniels, K. A., Bastow, I. D., Keir, D., Sparks, R. S. J., & Menand, T. (2014). Thermal models of dyke intrusion during development of continent–ocean transition. *Earth and Planetary Science Letters*, *385*, 145–153. https://doi.org/10.1016/j.epsl.2013.09.018

Doubre, C., Manighetti, I., Dorbath, C., Dorbath, L., Jacques, E., & Delmond, J. C. (2007). Crustal structure and magmato-tectonic processes in an active rift (Asal-Ghoubbet, Afar, East Africa): 1. Insights from a 5-month seismological experiment. *Journal of Geophysical Research: Solid Earth*, *112*(5), 1–22. https://doi.org/10.1029/2005JB003940

Drew, J., White, R. S., Tilmann, F., & Tarasewicz, J. (2013). Coalescence microseismic mapping. *Geophysical Journal International*, *195*(3), 1773–1785. https://doi.org/10.1093/gji/ggt331

Dugda, M. T. (2005). Crustal structure in Ethiopia and Kenya from receiver function analysis: Implications for rift development in eastern Africa. *Journal of Geophysical Research*, *110*(B1), B01303. https://doi.org/10.1029/2004JB003065

Ebinger, C. J., Keir, D., Ayele, A., Calais, E., Wright, T. J., Belachew, M., … Buck, W. R. (2008). Capturing magma intrusion and faulting processes during continental rupture: seismicity of the Dabbahu (Afar) rift. *Geophysical Journal International*, *174*(3), 1138–1152. https://doi.org/10.1111/j.1365-246X.2008.03877.x

Ebinger, C. J., & Casey, M. (2001). Continental breakup in magmatic provinces: An Ethiopian example. *Geology*, *29*(6), 527–530. https://doi.org/10.1130/0091-7613(2001)029<0527:CBIMPA>2.0.CO;2

Fontijn, K., Mcnamara, K., Zafu, A., Pyle, D. M., Dessalegn, F., Hutchison, W., … Yirgu, G. (2018). Contrasting styles of post-caldera volcanism along the Main Ethiopian Rift : Implications for contemporary volcanic hazards. *Journal of Volcanology and Geothermal Research*, *356*, 90–113. https://doi.org/10.1016/j.jvolgeores.2018.02.001

Foster, A. N., & Jackson, J. A. (1998). Source parameters of large African earthquakes: implications for crustal rheology and regional kinematics. *Geophysical Journal International*, *134*(2), 422–448. Retrieved from http://dx.doi.org/10.1046/j.1365-246x.1998.00568.x

Gíslason, G., Eysteinsson, H., Björnsson, G., & Harðardóttir, V. (2015). Results of Surface Exploration in the Corbetti Geothermal Area, Ethiopia. *World Geothermal Congress 2015*, (April), 1–10.

Grandin, R., Jacques, E., Nercessian, A., Ayele, A., Doubre, C., Socquet, A., … King, G. C. P. (2011). Seismicity during lateral dike propagation: Insights from new data in the recent Manda Hararo-Dabbahu rifting episode (Afar, Ethiopia). *Geochemistry, Geophysics, Geosystems*, *12*(4). https://doi.org/10.1029/2010GC003434

Greenfield, T., Keir, D., Kendall, J., & Ayele, A. (2018). Seismicity of the Bora- Tullu Moye volcanic field, 2016-2017. *Geochemistry, Geophysics, Geosystems*, 1–23. https://doi.org/10.1029/2018GC007648

Hayward, N. J., & Ebinger, C. J. (1996). Variations in the along-axis segmentation of the Afar Rift system. *Tectonics*, *15*(2), 244. https://doi.org/10.1029/95TC02292

Husen, S., Smith, R. B., & Waite, G. P. (2004). Evidence for gas and magmatic sources beneath the Yellowstone volcanic field from seismic tomographic imaging. *Journal of Volcanology and Geothermal Research*, *131*(3–4), 397–410. https://doi.org/10.1016/S0377-0273(03)00416-5

Hutchison, W., Biggs, J., Mather, T. A., Pyle, D. M., Lewi, E., Yirgu, G., … Fischer, T. P. (2016). Causes of unrest at silicic calderas in the East African Rift: New constraints from InSAR and soil-gas chemistry at Aluto volcano, Ethiopia. *Geochemistry, Geophysics, Geosystems*, *17*(8), 3008–3030. https://doi.org/10.1002/2016GC006395

Kebede, S. (2014). Geothermal Exploration and Development in Ethiopia: Country Update. *Short Course IX on Exploration for Geothermal Resources*, *15*, 8.

Keir, D., Stuart, G. W., Jackson, A., & Ayele, A. (2006). Local Earthquake Magnitude Scale and Seismicity Rate for the Ethiopian Rift. *Bulletin of the Seismological Society of America*, *96*(6), 2221–2230. https://doi.org/10.1785/0120060051

Keir, D., Ebinger, C. J., Stuart, G. W., Daly, E., & Ayele, A. (2006). Strain accommodation by magmatism and faulting as rifting proceeds to breakup: Seismicity of the northern Ethiopian rift. *Journal of Geophysical Research: Solid Earth*, *111*(B5). https://doi.org/10.1029/2005JB003748

Kissling, E., Kradolfer, U., & Maurer, H. (1995). Program VELEST user's guide-Short Introduction. *Institute of Geophysics, ETH Zurich*.

Korme, T., Acocella, V., & Abebe, B. (2004). The Role of Pre-existing Structures in the Origin, Propagation and Architecture of Faults in the Main Ethiopian Rift. *Gondwana Research*, *7*(2), 467–479. https://doi.org/10.1016/S1342-937X(05)70798-X

Lavayssière, A., Drooff, C., Ebinger, C., Gallacher, R., Illsley-Kemp, F., Oliva, S. J., & Keir, D. (2019). Depth Extent and Kinematics of Faulting in the Southern Tanganyika Rift, Africa. *Tectonics*. https://doi.org/10.1029/2018TC005379

Lin, G. (2013). Seismic investigation of magmatic unrest beneath Mammoth Mountain, California, USA. *Geology*, *41*(8), 847–850. https://doi.org/10.1130/G34062.1

Lin, G., & Shearer, P. M. (2009). Evidence for water-filled cracks in earthquake source regions. *Geophysical Research Letters*, *36*(17). https://doi.org/10.1029/2009GL039098

Lloyd, R., Biggs, J., Wilks, M., Nowacki, A., Kendall, J. M., Ayele, A., … Eysteinsson, H. (2018). Evidence for cross rift structural controls on deformation and seismicity at a continental rift caldera. *Earth and Planetary Science Letters*, *487*, 190–200.

https://doi.org/10.1016/j.epsl.2018.01.037

Lloyd, R., Biggs, J., Birhanu, Y., Wilks, M., Gottsmann, J., Kendall, J. M., … Eysteinsson, H. (2018). Sustained Uplift at a Continental Rift Caldera. *Journal of Geophysical Research: Solid Earth*, *123*(6), 5209–5226. https://doi.org/10.1029/2018JB015711

Lomax, A. (2008). The NonLinLoc software guide. *ALomax Scientific, Mouans-Sartoux, France, Http://Alomax. Free. Fr/Nlloc*.

Lomax, Anthony, Virieux, J., Volant, P., & Berge-Thierry, C. (2000). Probabilistic Earthquake Location in 3D and Layered Models BT - Advances in Seismic Event Location. In C. H. Thurber & N. Rabinowitz (Eds.) (pp. 101–134). Dordrecht: Springer Netherlands. https://doi.org/10.1007/978-94-015-9536-0_5

Mohr, P. A. (1966). Chabbi volcano (ethiopia). *Bulletin Volcanologique*, *29*(1), 797–815. https://doi.org/10.1007/BF02597195

Mohr, P., Mitchell, J. G., & Raynolds, R. G. H. (1980). Quaternary volcanism and faulting at O'A caldera, central ethiopian rift. *Bulletin Volcanologique*, *43*(1), 173. https://doi.org/10.1007/BF02597619

Nakajima, J., Matsuzawa, T., Hasegawa, A., & Zhao, D. (2001). Three-dimensional structure of Vp, Vs, and Vp/Vs beneath northeastern Japan: Implications for arc magmatism and fluids. *Journal of Geophysical Research: Solid Earth*, *106*(B10), 21843–21857. https://doi.org/10.1029/2000JB000008

Di Paola, G. M. (1971). Geology of the Corbetti Caldera area (Main Ethiopian Rift Valley). *Bulletin Volcanologique*, *35*(2), 497–506. https://doi.org/10.1007/BF02596970

Pérez-Gussinyé, M., Metois, M., Fernández, M., Vergés, J., Fullea, J., & Lowry, A. R. (2009). Effective elastic thickness of Africa and its relationship to other proxies for lithospheric structure and surface tectonics. *Earth and Planetary Science Letters*, *287*(1–2), 152–167. https://doi.org/10.1016/J.EPSL.2009.08.004

Pizzi, A., Coltorti, M., Abebe, B., Disperati, L., Sacchi, G., & Salvini, R. (2006). The Wonji fault belt (Main Ethiopian Rift): structural and geomorphological constraints and GPS monitoring. *Geological Society, London, Special Publications*, *259*(1), 191 LP – 207. https://doi.org/10.1144/GSL.SP.2006.259.01.16

Rapprich, V., Žáček, V., Verner, K., Erban, V., Goslar, T., Bekele, Y., … Hejtmánková, P. (2016). Wendo Koshe Pumice: The latest Holocene silicic explosive eruption product of the Corbetti Volcanic System (Southern Ethiopia). *Journal of Volcanology and Geothermal Research*, *310*, 159–171. https://doi.org/10.1016/j.jvolgeores.2015.12.008

Saria, E., Calais, E., Stamps, D. S., Delvaux, D., & Hartnady, C. J. H. (2014). Present-day kinematics of the East African Rift. *Journal of Geophysical Research: Solid Earth*, *119*(4), 3584–3600. https://doi.org/10.1002/2013JB010901

Scholz, C. H. (1988). The brittle-plastic transition and the depth of seismic faulting. *Geologische Rundschau*, 319–328.

Snoke, J. A. (1984). A program for focal mechanism determination by combined use of polarity and SV-P amplitude ratio data. *Earthquake Notes*, *55*, 15.

622 Stamps, D. S., Saria, E., & Kreemer, C. (2018). A Geodetic Strain Rate Model for the East
623 African Rift System. *Scientific Reports*, *8*(1), 732. https://doi.org/10.1038/s41598-017-
624 19097-w

625 Stuart, G. W., Bastow, I. D., & Ebinger, C. J. (2006). Crustal structure of the northern Main
626 Ethiopian Rift from receiver function studies. *Geological Society, London, Special*
627 *Publications*, 253–267.

628 Tarantola, A., & Valette, B. (1982). Generalized nonlinear inverse problems solved using the
629 least squares criterion. *Reviews of Geophysics*, *20*(2), 219–232.
630 https://doi.org/10.1029/RG020i002p00219

631 Le Turdu, C., Tiercelin, J.-J., Gibert, E., Travi, Y., Lezzar, K.-E., Richert, J.-P., … Taieb, M.
632 (1999). The Ziway–Shala lake basin system, Main Ethiopian Rift: Influence of volcanism,
633 tectonics, and climatic forcing on basin formation and sedimentation. *Palaeogeography,*
634 *Palaeoclimatology, Palaeoecology*, *150*(3–4), 135–177. https://doi.org/10.1016/S0031-
635 0182(98)00220-X

636 Watts, A. ., & Burov, E. . (2003). Lithospheric strength and its relationship to the elastic and
637 seismogenic layer thickness. *Earth and Planetary Science Letters*, *213*(1–2), 113–131.
638 https://doi.org/10.1016/S0012-821X(03)00289-9

639 Wilks, M., Kendall, J.-M., Nowacki, A., Biggs, J., Wookey, J., Birhanu, Y., … Bedada, T.
640 (2017). Seismicity associated with magmatism, faulting and hydrothermal circulation at
641 Aluto Volcano, Main Ethiopian Rift. *Journal of Volcanology and Geothermal Research*,
642 *340*, 52–67. https://doi.org/10.1016/J.JVOLGEORES.2017.04.003

643 Wilks, M., Ayele, A., Kendall, J. M., & Wookey, J. (2017). The 24th January 2016 Hawassa
644 earthquake: Implications for seismic hazard in the Main Ethiopian Rift. *Journal of African*
645 *Earth Sciences*, *125*(January 2016), 118–125.
646 https://doi.org/10.1016/j.jafrearsci.2016.11.007

647 WoldeGabriel, G., Walter, R. C., Aronson, J. L., & Hart, W. K. (1992). Geochronology and
648 distribution of silicic volcanic rocks of Plio-Pleistocene age from the central sector of the
649 Main Ethiopian Rift. *Quaternary International*, *13–14*, 69–76.
650 https://doi.org/10.1016/1040-6182(92)90011-P

651 Wolfenden, E., Ebinger, C., Yirgu, G., Deino, A., & Ayalew, D. (2004). Evolution of the
652 northern Main Ethiopian rift: birth of a triple junction. *Earth and Planetary Science Letters*,
653 *224*(1–2), 213–228. https://doi.org/10.1016/j.epsl.2004.04.022

654 Zhang, Q., & Lin, G. (2014). Three-dimensional Vp and Vp/Vs models in the Coso geothermal
655 area, California: Seismic characterization of the magmatic system. *Journal of Geophysical*
656 *Research: Solid Earth*, *119*(6), 4907–4922. https://doi.org/10.1002/2014JB010992

657